

THE DEFORMATION AND STABILITY OF AN ELASTIC CELL IN A UNIFORM FLOW*

ADAM A. YORKSTON[†], MARK G. BLYTH[†], AND EMILIAN I. PĂRĂU[†]

Abstract. The deformation and stability of a two-dimensional inextensible elastic cell in an inviscid uniform stream are investigated using a conformal mapping method. At low flow speeds equilibrium solutions are obtained using an asymptotic expansion, and the sequence of critical dimensionless pressures identified by Flaherty *et al.* (1972) for a circular cell exposed to a uniform transmural pressure is shown to play a crucial role. Below the smallest critical pressure a circular cell in a weak flow deforms into a near-elliptical shape with its major axis perpendicular to the flow, and above this critical pressure its major axis is aligned with the flow. At each subsequent critical pressure the bifurcations produce in alternating sequence cells with either one or two axes of symmetry. In the former case cells with left-right symmetry and cells with top-bottom symmetry are found. Equilibria for general flow speeds are calculated numerically, and their linear stability is analysed. Cells with two degrees of rotational symmetry whose longest chord is perpendicular to the uniform stream are found to be always stable. Other configurations are found to be stable only for certain parameter values. The nonlinear evolution of unstable cells subject to a small perturbation are computed numerically, and parameter values are located for which the cell falls into one of two distinct regular motions, either flipping over in alternating directions or bulging out to the side, while being intermittently propelled downstream with the flow.

Key words. hydroelasticity, potential flow, conformal mapping

AMS subject classifications. 74F10, 76B99, 76E99

1. Introduction. The study of the deformation of an elastic cell in response to a transmural pressure is a problem of fundamental interest. For a constant transmural pressure the problem was analysed by Lévy [7], Carrier [3] and Tadjbakhsh & Odeh [13]. Beyond a threshold pressure an initially circular cell eventually buckles into a shape with n -fold rotational symmetry. Flaherty *et al.* [5] extended the analysis to describe buckled elastic cells with a region of self-contact. Recent interest in the design and manufacture of inflatable aerofoils in the aviation industry [8, 6], which deform naturally in reaction to the air flow around them, motivates extending the problem when the cell is exposed to an ambient flow. A cell exposed to an inviscid flow experiences a non-constant transmural pressure that is unknown in advance and must be found simultaneously with the cell shape as part of the solution to the problem.

Here we conduct a fundamental study of the deformation of an inextensible elastic cell in an inviscid, irrotational uniform stream. The simpler case of a bubble in a uniform stream has been well studied. Equilibrium states were discussed by Vanden-Broeck & Keller [15], Shankar [12] and Tanveer [14] for example, and their linear stability was examined by Nie & Tanveer [9]. The recent study by Blyth & Părau [2] provided some preliminary insight into the elastic problem. Focusing on cell shapes which are both left-right symmetric and top-bottom symmetric, they used a linear expansion for the cell curvature to predict the first order deformation of an initially circular cell in a weak flow. Guided by these results they computed fully nonlinear equilibria using a numerical method based on a conformal mapping that is restricted to cells with a top-bottom cell symmetry.

We use the conformal mapping technique of Shankar [12], with no assumption of cell symmetry, to develop an asymptotic expansion in the flow speed parameter that allows corrections to be determined to any order, and we use this to identify

*Submitted to the editors January 4, 2019.

[†]School of Mathematics, University of East Anglia, Norwich, UK

novel solutions, expanding considerably on the previous results of Blyth & Părau [2]. We then extend these new solution branches to arbitrary flow speed numerically. Following Nie & Tanveer's [9] approach for the bubble problem, we determine the linear stability of the cell equilibria by formulating and solving an eigenvalue problem for the linear growth rates under a small amplitude perturbation. We reformulate the system to allow for an explicit time-stepping method to solve the nonlinear unsteady evolution of the cell, using Baumgarte stabilisation [1] to preserve the cell perimeter. We use this time-stepping scheme to verify the linear stability results, as well as to follow the evolution of a linearly unstable cell into the fully nonlinear regime. We create a stability map over parameter space to delineate the regions of dominance of certain linear growth rates, which can be used as a guide to the fully nonlinear unsteady motion.

The layout of the paper is as follows. In section 2 we formulate the problem and discuss the conformal mapping method. In section 3 we analyse steady state solutions via asymptotic and numerical methods. In section 4 we present some unsteady results. Finally, in section 5 we summarise our findings.

2. Formulation. We consider the deformation of a closed, two dimensional elastic cell placed in an inviscid, incompressible, irrotational fluid flow which is free from circulation. The cell wall is assumed to be massless and inextensible with constant thickness, and in the absence of an external pressure the cell is assumed to take the shape of a circle. The cell is assumed to have some uniform internal pressure $p_0(t)$, whose functional dependence is to be found, and the fluid flow is taken to be a horizontal uniform stream of speed U and pressure p_∞ in the far-field. Gravity is neglected.

Since the cell wall is massless, there must be a balance between the internal tension forces and the external pressure forces along an infinitesimal section of the cell wall. This force balance is given by

$$(2.1) \quad \frac{\partial}{\partial s} (T(s, t)\hat{\boldsymbol{\tau}} + N(s, t)\hat{\boldsymbol{n}}) + (p_0(t) - p(s, t))\hat{\boldsymbol{n}} = 0,$$

where $\hat{\boldsymbol{\tau}}$ and $\hat{\boldsymbol{n}}$ are unit vectors in the anticlockwise tangential and outward normal directions respectively, s is the arc-length of the cell wall in the anticlockwise direction, $p(s, t)$ is the external pressure acting on the cell wall, and $N(s, t)$ and $T(s, t)$ are the normal and tangential components respectively of the internal tension. Parametrising the cell wall as the vector $\boldsymbol{\eta}(s, t) = x(s, t)\mathbf{i} + y(s, t)\mathbf{j}$, we have the relations

$$(2.2) \quad \boldsymbol{\eta}_s = \hat{\boldsymbol{\tau}}, \quad \hat{\boldsymbol{\tau}}_s = \kappa\hat{\boldsymbol{n}}, \quad \hat{\boldsymbol{n}}_s = -\kappa\hat{\boldsymbol{\tau}},$$

where $\kappa = x_{ss}y_s - x_sy_{ss}$ is the signed curvature. Splitting (2.1) into tangential and normal components gives

$$(2.3) \quad T_s - \kappa N = 0, \quad N_s + \kappa T + p_0 - p = 0.$$

A balancing of moments about an infinitesimal section of the cell wall gives $N = M_s$, where M is the bending moment. We will assume the bending moment at any point is proportional to the difference between the curvature at that point and its resting curvature. Such an assumption is justified by Pozrikidis [10] for a locally inextensible cell. This gives the constitutive equation for the bending moment

$$(2.4) \quad M = -E_B(\kappa - \kappa_R),$$

where κ_R is the resting curvature, which is assumed to be constant, and E_B is the bending modulus. According to thin-shell theory, the bending modulus is given by $E_B = \frac{Eh^3}{12(1-\nu^2)}$, where E is the Young's modulus of the cell-wall, ν is the Poisson's ratio of the cell-wall, and h is the thickness of the cell-wall. The normal component of the tension is given by $N = M_s = -E_B\kappa_s$, which can be substituted into (2.3) to give

$$(2.5) \quad T_s + E_B\kappa\kappa_s = 0, \quad -E_B\kappa_{ss} + \kappa T + p_0 - p = 0.$$

We note in passing that when $E_B = 0$ equations (2.5) reduce to those for a bubble with constant surface tension. Integrating, we obtain

$$(2.6) \quad T = E_B \left(\frac{\sigma}{\ell^2} - \frac{1}{2}\kappa^2 \right), \quad p_0 - p = E_B \left(\kappa_{ss} + \frac{1}{2}\kappa^3 - \frac{\sigma\kappa}{\ell^2} \right),$$

where ℓ is a length scale taken to be the radius of the undeformed cell, and $\sigma(t)$ is some dimensionless function of time. As noted by Pozrikidis [10], (2.6) does not correspond to a constitutive equation for the tension T , but is simply an equilibrium condition. The function $\sigma(t)$ is determined implicitly by demanding that the perimeter of the cell is constant in time, and can be thought of as a Lagrange multiplier to enforce this constraint.

Next we consider the flow around the cell. Working in the complex z plane, where $z = x + iy$, and introducing the complex potential $w(z, t)$, we demand that the flow approaches the uniform stream with a finite pressure in the far-field by taking

$$(2.7) \quad w(z, t) - Uz \rightarrow 0 \quad \text{as} \quad |z| \rightarrow \infty.$$

We emphasise that this condition rules out any circulation. Comparing Bernoulli's equation between the surface of the cell and the far-field gives

$$(2.8) \quad \rho \Re \left(\frac{\partial w}{\partial t} \right) + \frac{1}{2}\rho q^2 + p = \frac{1}{2}\rho U^2 + p_\infty,$$

where ρ is the density of the fluid, $q = |\partial w / \partial z|$ is the flow speed, and all functions of space are evaluated on the surface of the cell. Using (2.6) to remove the surface pressure p , we obtain the governing equation on the surface of the cell

$$(2.9) \quad \rho \Re \left(\frac{\partial w}{\partial t} \right) + \frac{1}{2}\rho(q^2 - U^2) + p_0(t) - p_\infty - E_B \left(\kappa_{ss} + \frac{1}{2}\kappa^3 - \frac{\sigma\kappa}{\ell^2} \right) = 0,$$

where the internal pressure p_0 will later be shown to be time-dependent. We then non-dimensionalise, using the length scale ℓ , the radius of the undeformed cell, and taking the velocity scale to be $\sqrt{E_B/(\ell^3\rho)}$ and the time scale to be $\sqrt{\ell^5\rho/E_B}$. Equations (2.7) and (2.9) then become

$$(2.10) \quad w - \alpha z \rightarrow 0 \quad \text{as} \quad |z| \rightarrow \infty$$

and

$$(2.11) \quad \Re \left(\frac{\partial w}{\partial t} \right) + \frac{1}{2}(q^2 - \alpha^2) - (\kappa_{ss} + \frac{1}{2}\kappa^3 - \sigma\kappa) - P = 0,$$

where all variables are now dimensionless, and

$$(2.12) \quad \alpha = \sqrt{\frac{\ell^3\rho U^2}{E_B}}, \quad P(t) = \frac{(p_\infty - p_0(t))\ell^3}{E_B}$$

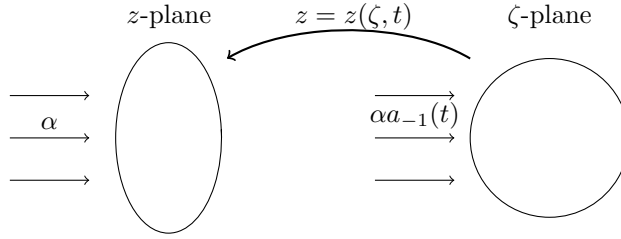


Fig. 1: Definition sketch showing the conformal mapping from the exterior of the unit circle in the ζ -plane to the exterior of the generally unsteady cell in the physical z -plane.

are dimensionless quantities relating to the far-field flow speed and the pressure difference between far-field and the interior of the cell respectively.

The kinematic condition requires that the speed of the fluid in the normal direction to the cell wall be equal to the normal component of the speed of the cell wall itself. In dimensionless terms, this can be written as

$$(2.13) \quad \boldsymbol{\eta}_t \cdot \hat{\mathbf{n}} = \mathbf{u} \cdot \hat{\mathbf{n}},$$

where \mathbf{u} is the fluid velocity. It will be convenient when working with complex notation to note that if we represent a vector $\mathbf{a} = (a_1, a_2)$, say, as the complex number $a = a_1 + ia_2$, then we can express the dot product $\mathbf{a} \cdot \mathbf{b}$ as $\Re(a\bar{b})$. In complex form, the unit tangent and normal vectors are $\boldsymbol{\tau} = \boldsymbol{\eta}_s$ and $\mathbf{n} = -i\boldsymbol{\eta}_s$ respectively, so the kinematic condition can be written in complex notation as

$$(2.14) \quad \Im(\boldsymbol{\eta}_t \bar{\boldsymbol{\eta}}_s) = \Im(u \bar{\boldsymbol{\eta}}_s).$$

Finally, since the cell wall is assumed to be inextensible, the perimeter must remain constant in time. Since the length scale has been taken to be the radius of the undeformed cell, the dimensionless perimeter must be 2π .

2.1. Conformal mapping. It is convenient to consider the cell in the physical z -plane as the image under a conformal mapping of the unit circle in the complex ζ -plane, as shown in figure 1. By the Riemann mapping theorem [4], at any point in time there exists a unique mapping $z(\zeta, t)$ from the exterior of the unit circle in the ζ plane to the exterior of the cell such that $z(\infty, t) = \infty$ and $z_\zeta(\infty, t) = a_{-1}(t) > 0$. The first point fixes the point at infinity, while the second condition fixes the rotational freedom of the Riemann mapping. The conformal mapping can thus be expanded as a Laurent series of the form

$$(2.15) \quad z(\zeta, t) = a_{-1}(t)\zeta + a_0(t) + \sum_{n=1}^{\infty} a_n(t)\zeta^{-n},$$

where a_{-1} is real and a_n are complex coefficients. Recalling the far-field condition (2.10), the complex potential in the ζ -plane, given in terms of the complex potential in the z -plane by $W(\zeta, t) \equiv w(z(\zeta, t), t)$, must take the form

$$(2.16) \quad W(\zeta, t) = \alpha a_{-1}(t)\zeta + \alpha a_0(t) + \sum_{n=1}^{\infty} b_n(t)\zeta^{-n}.$$

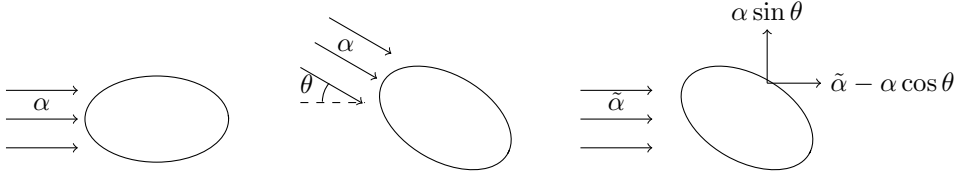


Fig. 2: Illustration to show how the rotation of a solution for a given α may be used to construct a new steadily translating solution for $\tilde{\alpha}$.

The partial derivatives of $w(z, t)$ are given in terms of $W(\zeta, t)$ and $z(\zeta, t)$ by

$$(2.17) \quad w_z(z, t) = \frac{W_\zeta(\zeta, t)}{z_\zeta(\zeta, t)}, \quad w_t(z, t) = W_t(\zeta, t) - \frac{W_\zeta(\zeta, t)z_t(\zeta, t)}{z_\zeta(\zeta, t)}.$$

Parametrising the unit circle in the ζ -plane as $\zeta = e^{i\phi}$, where $0 \leq \phi < 2\pi$, the cell wall $\eta(\phi, t) = z(e^{i\phi}, t)$ is then given by

$$(2.18) \quad \eta(\phi, t) = a_{-1}(t)e^{i\phi} + a_0(t) + \sum_{n=1}^{\infty} a_n(t)e^{-in\phi},$$

and the complex potential on the cell wall $\Omega(\phi, t) \equiv W(e^{i\phi}, t)$ is given by

$$(2.19) \quad \Omega(\phi, t) = \alpha a_{-1}(t)e^{i\phi} + \alpha a_0(t) + \sum_{n=1}^{\infty} b_n(t)e^{-in\phi},$$

with the flow speed on the cell-wall given by $q = \left| \frac{\partial w}{\partial z} \right| = |\Omega_\phi / \eta_\phi|$. Substituting these forms into (2.11), we obtain

$$(2.20) \quad \Re \left(\Omega_t - \frac{\Omega_\phi}{\eta_\phi} \eta_t \right) + \frac{1}{2}(q^2 - \alpha^2) - (\kappa_{ss} + \frac{1}{2}\kappa^3 - \sigma\kappa) - P = 0,$$

where $q = |\Omega_\phi / \eta_\phi|$. The kinematic condition (2.14) becomes

$$(2.21) \quad \Im(\bar{\eta}_\phi \eta_t) = -\Im(\Omega_\phi).$$

The inextensibility condition requires that the perimeter of the cell is 2π , which can be written as

$$(2.22) \quad \int_0^{2\pi} |\eta_\phi| d\phi = 2\pi.$$

We note that the area \mathcal{A} inside the cell is automatically conserved. Any change in area would require a point source/sink contribution in the far field, which is ruled out by condition (2.10). The area conservation can be seen directly by noting that

$$(2.23) \quad \frac{d\mathcal{A}}{dt} = \frac{d}{dt} \int_0^{2\pi} xy_\phi d\phi = - \int_0^{2\pi} \Im(\bar{\eta}_\phi \eta_t) d\phi,$$

which vanishes upon substitution of (2.21).

We also note that given a solution to the unsteady problem (2.20–2.22) for a chosen α , we can construct another unsteady solution for a different $\tilde{\alpha}$ by rotating the

system clockwise through an arbitrary angle θ and taking a reference frame moving with velocity $\mathbf{V} = (\alpha \cos \theta - \tilde{\alpha}, -\alpha \sin \theta)$, as is illustrated in figure 2. The new solution corresponds to the original cell motion with a superimposed steady translation of velocity $-\mathbf{V}$. This reflects the Galilean invariance of the physical system.

The system contains two forms of energy; the kinetic energy of the external fluid, and the internal bending energy of the cell. Because of the far-field uniform stream the kinetic energy of the fluid is infinite. Instead, we consider the system from a reference frame moving at speed α in the direction of the flow. In this reference frame the fluid in the far-field is stationary, hence the dimensionless kinetic energy of the fluid is finite, given by

$$\begin{aligned}
 \mathcal{K} &= \iint \frac{1}{2} |\mathbf{u} - \alpha \mathbf{i}|^2 dx dy \\
 (2.24) \quad &= \iint \frac{1}{2} \nabla \cdot (\Re(w - \alpha z) \nabla (\Re(w - \alpha z))) dx dy \\
 &= -\frac{1}{2} \int_0^{2\pi} \Re(\Omega - \alpha \eta) \Im(\Omega_\phi - \alpha \eta_\phi) d\phi,
 \end{aligned}$$

where the double integral in (2.24) is taken over the region outside the cell. The dimensionless bending energy of the cell is given by

$$(2.25) \quad \mathcal{W} = \int_0^{2\pi} \frac{1}{2} (\kappa + 1)^2 |\eta_\phi| d\phi,$$

where the resting cell with curvature $\kappa = -1$ has zero bending energy. We note that the bending energy of the cell depends only on its shape, and not on its speed or position, and so is independent of reference frame. It is straightforward to show that the total energy of the system $\mathcal{E} = \mathcal{K} + \mathcal{W}$ is an invariant of the motion. This has a minimum of $\mathcal{E} = 0$, which corresponds to a circular cell moving at constant speed α with the flow.

2.2. The steady system. For steady flow, the system given by (2.20)–(2.22) reduces to

$$(2.26) \quad \frac{1}{2}(q^2 - \alpha^2) - (\kappa_{ss} + \frac{1}{2}\kappa^3 - \sigma\kappa) - P = 0,$$

$$(2.27) \quad \Im(\Omega_\phi) = 0,$$

$$(2.28) \quad \int_0^{2\pi} \left| \frac{d\eta}{d\phi} \right| d\phi = 2\pi,$$

where here the pressure difference P is taken to be a parameter. Noting that the choice of a_0 simply corresponds to a translation of the cell in the ζ -plane, we are free to choose $a_0 = 0$ without loss of generality. We can then rewrite $z(\zeta)$ and $\eta(\phi)$ as

$$(2.29) \quad z(\zeta) = a_{-1} \left(\zeta + \sum_{n=1}^{\infty} \frac{a_n}{\zeta^n} \right), \quad \eta(\phi) = a_{-1} \left(e^{i\phi} + \sum_{n=1}^{\infty} a_n e^{-in\phi} \right),$$

where the coefficients a_n have now been rescaled by the real coefficient a_{-1} . The constant a_{-1} can be determined in terms of the mapping coefficients a_n by enforcing (2.28),

$$(2.30) \quad 2\pi = \int_0^{2\pi} \left| \frac{d\eta}{d\phi} \right| d\phi = a_{-1} \int_0^{2\pi} \left| e^{i\phi} - \sum_{n=1}^{\infty} n a_n e^{-in\phi} \right| d\phi,$$

giving

$$(2.31) \quad a_{-1} = \frac{2\pi}{\int_0^{2\pi} |e^{i\phi} - \sum_{n=1}^{\infty} na_n e^{-in\phi}| d\phi}.$$

The kinematic condition (2.27) ensures that the cell wall is a streamline. In terms of the complex potential (2.19), this can be written as $b_1 = \alpha a_{-1}$, $b_n = 0$ for $n \geq 2$, reducing the complex potential to

$$(2.32) \quad W(\zeta) = \alpha a_{-1} \left(\zeta + \frac{1}{\zeta} \right), \quad \Omega(\phi) = 2\alpha a_{-1} \cos \phi,$$

a uniform flow around the unit circle in the ζ -plane. It is clear from (2.26) and (2.32) that the problem is invariant under the transformation $\alpha \mapsto -\alpha$; physically this simply corresponds to reversing the flow direction.

We now have a mapping from the flow in the ζ -plane to the z -plane that satisfies both the kinematic condition (2.27) and the perimeter normalisation (2.28), thus reducing the problem to solving (2.26) in terms of the mapping coefficients a_n , a nonlinear algebraic equation.

The numerical method used to compute nonlinear steady solutions is based on that presented by Tanveer [14], which was used to compute solutions to the problem of a bubble with surface tension in a uniform flow. We note that since the Fourier series representation of $\eta(\phi)$ in (2.29) represents a smooth periodic function of ϕ , the coefficients $a_n(t)$ tend to zero faster than any power of n , which means we have spectral convergence (see Theorem 9.5.3 in [11]). We truncate the mapping function to N terms, setting $a_n = 0$ for $n > N$. We then split up the coefficients of the mapping function a_n into real and imaginary parts, giving $2N$ real variables, where a_{-1} is taken as a function of a_n using (2.31). The parameters α and P are fixed, while σ is to be found as part of the solution, giving $2N + 1$ unknowns. We can then obtain expressions for κ , κ_{ss} and q for this truncated mapping as functions of ϕ in terms of the mapping coefficients a_n , where all derivatives are found analytically. We then evaluate (2.26) at $2N + 1$ equally spaced collocation points $\phi_i = 2\pi(i - 1)/(2N + 1)$, for $i = 1, \dots, 2N + 1$, giving $2N + 1$ equations to solve for the $2N + 1$ variables. The Jacobian of this system is found analytically, and Newton's method is used to find a numerical solution. For the results shown in this section, we generally take $N = 200$, although values as high as $N = 2000$ are required for certain solutions. To check the accuracy of the results we recall that, for any given mapping function, we can find the absolute error in satisfying (2.26) analytically along the entire cell, not just at the $2N + 1$ collocation points used in Newton's method. So we can verify the validity of our results by sampling (2.26) at a much larger number of points, say $1000N$, and confirm this error remains small. All results in this work have a maximum absolute error less than 10^{-10} . For the initial guess for Newton's method, we use the small α asymptotic results presented below to reach the desired solution branch. By slowly varying the parameters α and P , we can then explore the full nonlinear solution space.

2.3. Nonlinear time-evolution. The time-dependent system is given by equations (2.20), (2.21) and (2.22). This set of equations implicitly governs the evolution in time of an initial flow state. Although this implicit system can be solved numerically, it is convenient to work with a more explicit form. We make use of the method by [9], used to obtain an explicit system for the unsteady motion of a bubble in a

uniform stream. We start by rewriting the kinematic condition (2.21) in the form

$$(2.33) \quad -\Re\left(\frac{i\Omega_\phi}{|\eta_\phi|^2}\right) = \Re\left(\frac{i\eta_t}{\eta_\phi}\right) = \Re\left(\frac{z_t}{\zeta z_\zeta}\right)\Big|_{\zeta=e^{i\phi}}.$$

Since $z_t/\zeta z_\zeta$ is analytic in $|\zeta| > 1$, it can be represented as a Laurent expansion about $\zeta = 0$ with only negative powers. Evaluating this expansion at $\zeta = e^{i\phi}$, it can be shown that

$$(2.34) \quad \eta_t = i\eta_\phi \Re\left(\frac{i\Omega_\phi}{|\eta_\phi|^2}\right) - \eta_\phi \mathcal{H}\left(-\Re\left(\frac{i\Omega_\phi}{|\eta_\phi|^2}\right)\right),$$

where \mathcal{H} is the Hilbert transform. Since $\Omega_t - \Omega_\phi \eta_t / \eta_\phi = (W_t - W_\zeta z_t / z_\zeta)|_{\zeta=e^{i\phi}}$ where $W_t - W_\zeta z_t / z_\zeta$ is analytic in $|\zeta| > 1$, (2.20) can be rewritten as

$$(2.35) \quad \begin{aligned} \Omega_t &= \frac{\Omega_\phi}{\eta_\phi} \eta_t - \frac{1}{2}(q^2 - \alpha^2) + (\kappa_{ss} + \frac{1}{2}\kappa^3) + P \\ &+ i\mathcal{H}\left(\frac{1}{2}q^2 - \kappa_{ss} - \frac{1}{2}\kappa^3\right) - \sigma(\kappa - i\mathcal{H}(\kappa)). \end{aligned}$$

We now have explicit expressions for η_t and Ω_t , with $P(t)$ and $\sigma(t)$ still to be determined. The value of P can be determined, up to a linear dependency on σ , by noting that the mean value of $\Omega_t - \Omega_\phi \eta_t / \eta_\phi$ around the cell wall is zero, hence $P(t)$ must be taken to be

$$(2.36) \quad P = \frac{1}{2\pi} \int_0^{2\pi} \left[\frac{1}{2}(q^2 - \alpha^2) - (\kappa_{ss} + \frac{1}{2}\kappa^3 - \sigma\kappa)\right] d\phi.$$

To determine the value of $\sigma(t)$, we need to consider the inextensibility condition

$$(2.37) \quad L(t) = \int_0^{2\pi} \left|\frac{\partial\eta}{\partial\phi}\right| d\phi = 2\pi,$$

where $L(t)$ is the perimeter of the cell. The value of σ only indirectly affects the value of $L(t)$, but recalling the vector relations $\boldsymbol{\eta}_\phi = |\eta_\phi|\boldsymbol{\tau}$, $\boldsymbol{\tau}_\phi = \kappa|\eta_\phi|\boldsymbol{n}$, as well as the kinematic condition on the boundary $\boldsymbol{\eta}_t \cdot \boldsymbol{n} = \Im(\Omega_\phi)/|\eta_\phi|$, we have

$$(2.38) \quad \frac{\partial}{\partial t} \left|\frac{\partial\eta}{\partial\phi}\right| = \boldsymbol{\eta}_{\phi t} \cdot \boldsymbol{\tau} = \frac{\partial}{\partial\phi} (\boldsymbol{\eta}_t \cdot \boldsymbol{\tau}) - \kappa|\eta_\phi|\boldsymbol{\eta}_t \cdot \boldsymbol{n} = \frac{\partial}{\partial\phi} (\boldsymbol{\eta}_t \cdot \boldsymbol{\tau}) - \kappa\Im(\Omega_\phi),$$

and so we obtain

$$(2.39) \quad L'(t) = \frac{\partial}{\partial t} \int_0^{2\pi} |\eta_\phi| d\phi = \int_0^{2\pi} \kappa_\phi \Im(\Omega) d\phi,$$

and

$$(2.40) \quad L''(t) = \int_0^{2\pi} [\kappa_\phi \Im(\Omega_t) - \kappa_t \Im(\Omega_\phi)] d\phi,$$

where $\Im(\Omega_t)$ is given explicitly by

$$(2.41) \quad \Im(\Omega_t) = \Im\left(\frac{\Omega_\phi}{\eta_\phi} \eta_t\right) + \mathcal{H}\left(\frac{1}{2}q^2 - \kappa_{ss} - \frac{1}{2}\kappa^3\right) + \sigma\mathcal{H}(\kappa).$$

We can thus fix the value of $L''(t)$ with an appropriate choice of $\sigma(t)$ by taking

$$(2.42) \quad \sigma = \frac{L''(t) - \int_0^{2\pi} \left[\kappa_\phi \Im \left(\frac{\Omega_\phi}{\eta_\phi} \eta_t \right) + \kappa_\phi \mathcal{H} \left(\frac{1}{2} q^2 - \kappa_{ss} - \frac{1}{2} \kappa^3 \right) - \kappa_t \Im(\Omega_\phi) \right] d\phi}{\int_0^{2\pi} \kappa_\phi \mathcal{H}(\kappa) d\phi}.$$

A natural choice would be to set $L''(t) = 0$ with initial conditions $L(0) = 2\pi$, $L'(0) = 0$, which satisfies the inextensibility condition $L(t) = 2\pi$. However, such a choice is not numerically stable; a small error in $L''(t)$ results in quadratic growth of $L(t)$. To avoid this, we use the Baumgarte stabilisation method [1] by setting

$$(2.43) \quad L''(t) = -2\gamma L'(t) - \gamma^2(L(t) - 2\pi),$$

where γ is some large positive constant. This condition is analytically equivalent to $L(t) = 2\pi$ with the initial conditions $L(0) = 2\pi$, $L'(0) = 0$, but results in a numerically stable system.

To compute the time evolution of unsteady solutions, we truncate the mapping (2.15) by setting $a_n = b_n = 0$ for $n > N$, where N is a chosen truncation value, and evaluate equations (2.34) and (2.35) at some M equally spaced collocation points ϕ_i to obtain η_t and Ω_t . The Hilbert transform appearing in (2.34) and (2.35) is computed in Fourier space by using the well-known result

$$\mathcal{H}(e^{in\phi}) = -i \operatorname{sgn}(n) e^{in\phi} \text{ for } n \neq 0.$$

The values $a'_n(t)$ and $b'_n(t)$ can then be obtained by a Fourier transform, reducing the problem to a system of $2N + 2$ ODEs for the variables a_{-1} , a_0 , a_n , b_n , where $n = 1 \dots N$. The system is then solved in MATLAB using the function `ode113`, which uses an Adams-Bashforth-Moulton method. To ensure the validity of the results over the time-scales considered, the truncation levels were taken at $N = 50$, $N = 60$ and $N = 70$ and it was confirmed that the results converge as N is increased. At each time-step, the number of collocation points was set at both $M = 128$ and $M = 256$ and compared to ensure the values of $a'_n(t)$ and $b'_n(t)$ did not vary by more than 10^{-8} . Recalling from §2.1 that the perimeter and area inside the cell and the total energy \mathcal{E} are all conserved quantities of the system, we can use the numerical deviation of these quantities to give an indication of the scale of the numerical error. The stabilisation factor γ is taken to be 10^4 for all computations, which keeps the absolute error of the perimeter to within 10^{-6} . This is found to be the biggest source of error in the computations, but is sufficient for small-time computations and qualitative study of long-time behaviour.

2.4. Linear Stability. To study the linear stability of the steady solutions, we introduce a small perturbation to both the cell boundary and the flow itself, writing $\eta(\phi, t) = \eta^s(\phi) + \hat{\eta}(\phi, t)$, $\Omega(\phi, t) = \Omega^s(\phi) + \hat{\Omega}(\phi, t)$, $\sigma(t) = \sigma^s + \hat{\sigma}(t)$, $P = P^s + \hat{P}(t)$, where superscript s indicates the steady solution, and hats indicate small time-dependent perturbations. Substituting these perturbations into the time-dependent system (2.20)–(2.22), we obtain the linearised system

$$(2.44) \quad \Im(\hat{\eta}_t \bar{\eta}_\phi^s) = -\Im(\hat{\Omega}_\phi),$$

$$(2.45) \quad \Re\left(\hat{\Omega}_t - \frac{\Omega_\phi^s}{\eta_\phi^s} \hat{\eta}_t\right) = 2 \frac{\Re(\hat{\Omega}_\phi \bar{\Omega}_\phi^s)}{|\eta_\phi^s|^2} - 2 \frac{|\Omega_\phi^s|^2}{|\eta_\phi^s|^4} \Re(\hat{\eta}_\phi \bar{\eta}_\phi^s) + \hat{\kappa}_{ss} + \frac{3}{2} (\kappa^s)^2 \hat{\kappa} - \sigma^s \hat{\kappa} - \hat{\sigma} \kappa^s + \hat{P},$$

$$(2.46) \quad \int_0^{2\pi} \kappa^s \Im \left(\hat{\Omega}_{\phi t} \right) d\phi = 0.$$

The mapping coefficients for the perturbed flow can be written as $a_n(t) = a_n^s + \hat{a}_n(t)$, $b_n(t) = b_n^s + \hat{b}_n(t)$. We then truncate the perturbed mapping functions at \hat{a}_N and \hat{b}_N , and split the mapping coefficients into real and imaginary parts. Noting that a_{-1} , P and σ are real, we have $4N + 5$ unknowns, corresponding to \hat{a}_{-1} , \hat{P} , $\hat{\sigma}$, and the real and imaginary parts of \hat{a}_n and \hat{b}_n . We evaluate (2.44) and (2.45) at $2N + 2$ equally spaced collocation points ϕ_i , which together with (2.46) gives $4N + 5$ equations for the $4N + 5$ unknowns. These equations can then be written as the linear system

$$(2.47) \quad \mathbf{A}\mathbf{X}' = \mathbf{B}\mathbf{X},$$

where $\mathbf{X}(t)$ contains the $4N + 5$ unknowns, and \mathbf{A} and \mathbf{B} are $(4N + 5) \times (4N + 5)$ matrices whose elements are known explicitly in terms of a_n^s , b_n^s , σ^s . Seeking normal mode solutions of the form $\mathbf{X}(t) = \mathbf{X}_0 e^{\lambda t}$, we obtain the generalised eigenvalue problem $\lambda \mathbf{A}\mathbf{X}_0 = \mathbf{B}\mathbf{X}_0$, which we solve numerically using the in-built Matlab `eig` function. Since the matrices \mathbf{A} and \mathbf{B} are real, the eigenvalues λ must come in complex conjugate pairs $\{\lambda, \bar{\lambda}\}$, with corresponding eigenvectors $\{\mathbf{v}, \bar{\mathbf{v}}\}$. These eigenvectors are in general complex, but real solutions to (2.47) can be constructed by taking $\mathbf{X} = r(\mathbf{v} \exp(\lambda t + ik) + \bar{\mathbf{v}} \exp(\bar{\lambda} t - ik))$, where r and k are freely chosen real numbers corresponding to the magnitude and phase-shift of the perturbation respectively. A steady solution is said to be spectrally stable if $\Re(\lambda) \leq 0$ for all eigenvalues λ , and unstable otherwise.

The steady solution at $(\alpha + \hat{\alpha}, P)$ can be considered a perturbation of the steady solution at (α, P) which has a different cell shape and correspondingly a different flow. Also, we know from §2.1 that a steady solution at some $\alpha + \hat{\alpha}$ can be considered a steadily translating solution at α , where the direction of the translation can be freely chosen. Hence for a steady solution at (α, P) there always exist perturbations of the form $\hat{\eta}(\phi, t) = (a + bi)t + C_1(\phi)$, $\hat{\Omega}(\phi, t) = C_2(\phi)$, where a and b are freely chosen constants, and $C_1(\phi)$ and $C_2(\phi)$ are associated with the change in shape and the corresponding flow change respectively. With reference to (2.47) these perturbations can be expressed as a linear combination of the two perturbations $\mathbf{X}_1 = \mathbf{v}_1 t + \mathbf{w}_1$ and $\mathbf{X}_2 = \mathbf{v}_2 t + \mathbf{w}_2$, where \mathbf{v}_1 corresponds to a perturbation of $\Re(a_0)$ only and is a horizontal translation, and \mathbf{v}_2 corresponds to a perturbation of $\Im(a_0)$ only and is a vertical translation. Substituting these expressions into the linear system (2.47), we obtain $\mathbf{B}\mathbf{v}_n = 0$, $\mathbf{B}\mathbf{w}_n = \mathbf{A}\mathbf{v}_n$ for $n = 1, 2$. So the two linearly independent \mathbf{v}_n are eigenvectors, with generalised eigenvectors \mathbf{w}_n of rank 2, corresponding to a zero eigenvalue. The steady solution at $(\alpha, P + \hat{P})$ can also be considered a perturbation of the steady solution at (α, P) , which has a different shape and correspondingly a different flow. Since this perturbation is time-independent, it also corresponds to an eigenvector with zero eigenvalue. We conclude that (2.47) has a zero eigenvalue with three linearly independent eigenvectors and two linearly independent generalised eigenvectors of rank 2, which implies algebraic multiplicity five and geometric multiplicity three. This agrees with the results obtained numerically.

Since the full system (2.20)-(2.22) is invariant under the transform $\eta(\phi, t) \rightarrow -\bar{\eta}(\pi - \phi, -t)$, $\Omega(\phi, t) \rightarrow -\bar{\Omega}(\pi - \phi, -t)$, if a steady solution has eigenvalue λ then its reflection about a vertical axis is another steady solution with eigenvalue $-\lambda$. Furthermore, if the steady solution is left-right symmetric its eigenvalues will appear as quadruples $\{\lambda, \bar{\lambda}, -\lambda, -\bar{\lambda}\}$ and in this case stability can only occur if $\Re(\lambda) = 0$ for all eigenvalues λ .

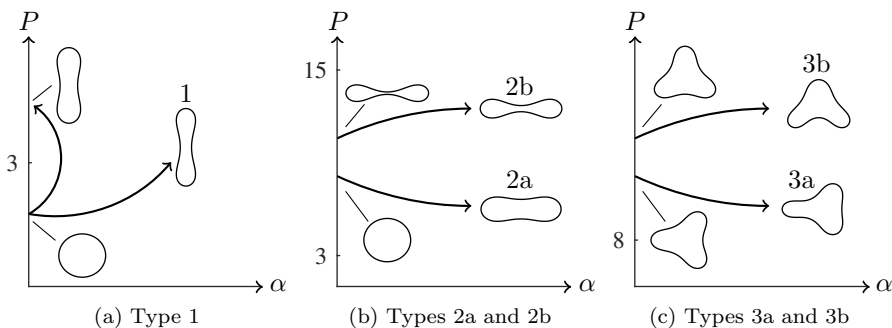


Fig. 3: Sketch showing the classification of the steady solutions in relation to those at $\alpha = 0$. The arrows illustrate a continuous path taken to reach a particular cell type. The cells in a static fluid at $\alpha = 0$ are also shown.

3. Steady state analysis. In this section we discuss steady solutions obtained both analytically and numerically, and determine their linear stability. As shown in §2.2 the steady solutions are governed by

$$(3.1) \quad \frac{1}{2}(q^2 - \alpha^2) - (\kappa_{ss} + \frac{1}{2}\kappa^3 - \sigma\kappa) - P = 0,$$

where the cell wall and complex potential along the cell wall are given by

$$(3.2) \quad \eta(\phi) = a_{-1} \left(e^{i\phi} + \sum_{n=1}^{\infty} a_n e^{-in\phi} \right), \quad \Omega(\phi) = 2\alpha a_{-1} \cos \phi,$$

where a_{-1} is given by (2.31).

To describe the behaviour of the steady solutions as the parameters α and P vary, it is useful to label the solutions in terms of those found at $\alpha = 0$. The case of $\alpha = 0$, an elastic cell in a stationary fluid, is well studied, notably by Flaherty *et al.* [5], who showed that as well as a circular cell solution, there exist buckled mode- k solutions bifurcating from the circular solution at critical pressures $P = k^2 - 1$ for $k \geq 2$.

Since cell orientation matters when α is non-zero, we will use the terms horizontally aligned and vertically aligned to refer to cells whose longest axis is parallel and perpendicular to the flow direction respectively.

For $\alpha = 0$ and $P < 3$, there is only the circular solution. We label as type 1 those solutions that can be obtained by continuously varying P and α from the circular state at $\alpha = 0$, $P < 3$. This is illustrated in figure 3a by following one of the arrows from $\alpha = 0$. Note that since $(\alpha, P) = (0, 3)$ is a bifurcation point, we exclude the possibility of passing through this point in this definition. By numerically following a particular type 1 branch to $\alpha = 0$ and $P > 3$, we find that we obtain the vertically aligned buckled mode-2 solution, which must therefore also be of type 1.

For $\alpha = 0$ and $3 < P < 8$, there exist both a buckled mode-2 solution and a circular solution. In the absence of a flow, these mode-2 solutions can take any orientation. However, as α is increased from zero only the horizontally and vertically aligned cells persist. We have already seen that the vertically aligned mode-2 cells are of type 1. We label as type 2a or type 2b any solution which has both top-bottom and left-right symmetry and which, on following a continuous path in the $\alpha - P$ plane to

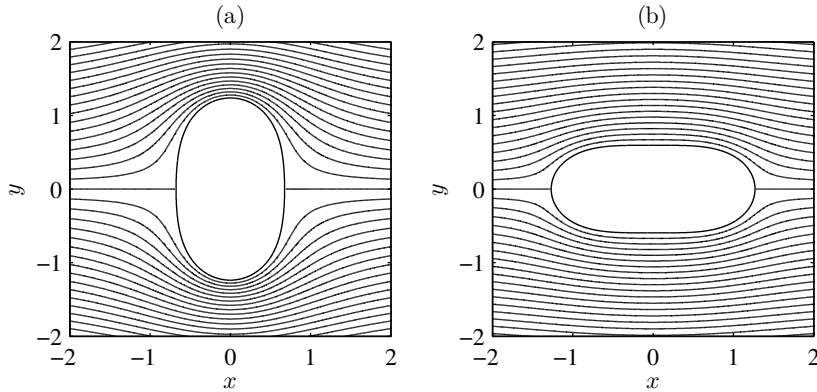


Fig. 4: Streamline plots for solutions at $\alpha = 1$ for the type 1 (left) and type 2a (right) solutions at $P = 2$ and $P = 4$ respectively.

a point $\alpha = 0$ with $3 < P < 15$, arrives at the circular state or the horizontal mode-2 solution respectively, as shown in figure 3b. By numerically following a particular type 2a branch to $\alpha = 0$ and $P > 15$, we find that we obtain the buckled mode-4 solution, which must therefore also be of type 2a. The other orientation of the buckled mode-4 solution, as well as the circular solution at $P > 15$, form solution branches separate from those previously defined, and will not be considered in the present work.

For $\alpha = 0$ and $8 < P < 15$, as well as the circular and mode-2 solutions there also exists a buckled mode-3 solution. As α is increased, we find that four orientations of this mode-3 solution persist: the two left-right symmetric orientations, and the two top-bottom symmetric orientations. Due to the symmetry of the problem, the two left-right symmetric orientations are top-bottom reflections of each other, and the two top-bottom symmetric orientations are left-right reflections of each other. We label as type 3a any solution with top-bottom symmetry and left-right asymmetry which, on following a continuous path in the $\alpha - P$ plane to a point $\alpha = 0$ with $P > 8$, arrives at a buckled mode-3 solution, as shown in figure 3c. Similarly we label as type 3b any solution which has left-right symmetry and top-bottom asymmetry which, on following a continuous path in the $\alpha - P$ plane to a point $\alpha = 0$ with $P > 8$, arrives at a buckled mode-3 solution.

For $\alpha = 0$ and $P > 15$ there exist mode-4 buckled solutions, and in general for $P > k^2 - 1$ there exist mode- l solutions for all $l \leq k$. In this work we focus mainly on the type 1, 2a, 2b, 3a and 3b cases as defined above. Solutions stemming from higher mode buckled solutions can however be studied using the same techniques.

3.1. Small α analysis. We now seek asymptotic expansions for $\alpha \ll 1$ for solution branches stemming from the unit circle at $\alpha = 0$. Since (3.1) is invariant under the transformation $\alpha \mapsto -\alpha$, we expand the unknowns in powers of α^2 as

$$(3.3) \quad a_{-1} = 1 + \alpha^2 a_{-1,1} + \alpha^4 a_{-1,2} + \dots,$$

$$(3.4) \quad a_n = \alpha^2 a_{n,1} + \alpha^4 a_{n,2} + \dots \quad (n \geq 1),$$

$$(3.5) \quad \sigma = \frac{1}{2} - P + \alpha^2 \sigma_1 + \alpha^4 \sigma_2 + \dots,$$

where $a_{-1} = 1$, $a_n = 0$, $\sigma = \frac{1}{2} - P$ is the circular solution at $\alpha = 0$. We then

substitute these expressions into (2.31), (3.1) and (3.2), which can be solved at each order α^{2m} to obtain the values of $a_{-1,m}$, $a_{n,m}$ and σ_m . Note that although the results in this section are only shown to $O(\alpha^2)$, the method can be used to obtain results to any order. These can then be compared to the numerical results to confirm their accuracy.

At $O(\alpha^2)$, we find that (2.31) gives $a_{-1,1} = 0$, and (3.1) gives

$$(3.6) \quad \frac{1}{2} - \sigma_1 - \cos 2\phi + \sum_{n=2}^{\infty} (n^2 - 1)(P - n^2 + 1) \{ \Re(a_{n-1,1}) \cos n\phi + \Im(a_{n-1,1}) \sin n\phi \} = 0.$$

So $\sigma_1 = \frac{1}{2}$, and comparing coefficients of $\cos 2\phi$ and $\sin 2\phi$ in (3.6) we find that $a_{1,1}$ is real and satisfies

$$(3.7) \quad 3(P - 3)a_{1,1} = 1.$$

For $P = 3$, (3.7) clearly has no solutions. However Blyth & Părău [2] found that solutions can be found by taking an expansion in $\alpha^{2/3}$. Following this approach here we find that

$$(3.8) \quad \eta(\phi) = e^{i\phi} - \frac{2}{9} \sqrt[3]{12} \alpha^{2/3} e^{-i\phi} + O(\alpha^{4/3})$$

so that, ignoring the $O(\alpha^{4/3})$ correction, the cell is an ellipse with its major axis aligned perpendicular to the flow. This corresponds to a type 1 solution, and agrees with that found by Blyth & Părău [2].

Henceforth we assume that $P \neq 3$. Comparing coefficients of $\cos n\phi$ and $\sin n\phi$ in (3.6), we have

$$(3.9) \quad (P - n^2 + 1)a_{n-1,1} = 0 \quad \text{for } n \geq 3.$$

So if $P \neq k^2 - 1$ for all $k \geq 3$ we must have $a_{n,1} = 0$ for $n \geq 2$ in which case

$$(3.10) \quad \eta(\phi) = e^{i\phi} + \frac{\alpha^2}{3(P - 3)} e^{-i\phi} + O(\alpha^4),$$

which is approximately an ellipse. For $P < 3$, the cell is aligned perpendicular to the flow, which corresponds to a type 1 solution. For $P > 3$, the cell is aligned parallel with the flow, corresponding to a type 2a solution. Figure 4 shows the streamlines for both of these solutions calculated numerically by solving the full problem using the method described in section 3.2. Considering higher order terms, we find that at $O(\alpha^4)$, this solution has a singularity at $P = 15$, and in general at $O(\alpha^{2m})$ a singularity occurs at $P = 4m^2 - 1$ for integer $m \geq 2$. However, unlike at $P = 3$, expansions at these critical pressures can be constructed involving only even integer powers and so a cusp in the energy curve is not expected.

In general if $P = k^2 - 1$ for some $k \geq 3$, then (3.7) requires $a_{1,1} = 1/(3P - 9)$, and (3.9) requires $a_{n-1,1} = 0$ for $n \geq 3$ with $n \neq k$, but $a_{k-1,1}$ is as yet unknown. In fact $a_{k-1,1}$ can only be determined by considering higher order terms in α . This can be done by continuing in the same vein as before; however, it is more informative to note that the expansion for the curvature takes the form

$$(3.11) \quad \kappa = -1 - \left((k^2 - 1)(C_{r1} \cos k\phi + C_{i1} \sin k\phi) + \frac{\cos 2\phi}{k^2 - 4} \right) \alpha^2 + \kappa_2(\phi) \alpha^4 + O(\alpha^6),$$

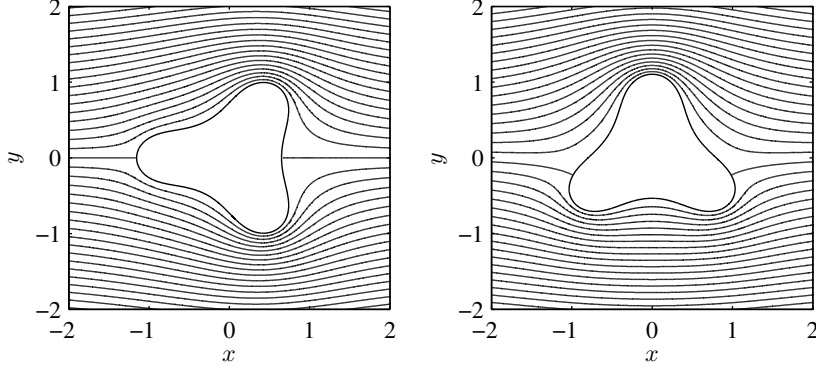


Fig. 5: Streamline plots for the type 3a (left) and type 3b (right) solutions at $\alpha = 1$, $P = 10$.

where $C_{r1} = \Re(a_{k-1,1})$, $C_{i1} = \Im(a_{k-1,1})$ and $\kappa_2(\phi)$ is as yet unknown. Substituting into (3.1) and considering the $O(\alpha^4)$ terms, we obtain

$$(3.12) \quad \kappa_2'' + k^2 \kappa_2 = -\frac{(4k^2 - 1) \cos 4\phi}{12(k^2 - 4)^2} - \frac{1}{2}(k-1)(k-3) (C_{r1} \cos k\phi + C_{i1} \sin k\phi) + \dots,$$

where a prime indicates a derivative in ϕ and all of the terms on the right hand side which cannot cause a resonance have been omitted for brevity. Resonances cannot be permitted since we demand solutions which are periodic in ϕ . Therefore for $k \geq 5$, we must have $C_{r1} = C_{i1} = 0$ and the cell shape is given by (3.10). For $k = 4$ we must have $C_{r1} = -7/288$ and $C_{i1} = 0$, so that the cell shape is

$$(3.13) \quad \eta(\phi) = e^{i\phi} + \frac{\alpha^2}{36} \left(e^{-i\phi} - \frac{7}{8} e^{-3i\phi} \right) + O(\alpha^4).$$

For $k = 3$, the resonant terms vanish, so C_{r1} and C_{i1} remain undetermined. We will have to go to higher order to determine these constants. So taking $k = 3$, we proceed as before, and find that to remove the resonances at $O(\alpha^6)$ we must have

$$(3.14) \quad C_{r1} \left(C_{r1}^2 + C_{i1}^2 - \frac{201}{102400} \right) = 0, \quad C_{i1} \left(C_{r1}^2 + C_{i1}^2 - \frac{201}{102400} \right) = 0,$$

and to remove the resonances at $O(\alpha^8)$ we must have

$$(3.15) \quad \frac{201}{102400} C_{i2} - 2C_{i1} C_{r1} C_{r2} - \frac{29}{1152} C_{i1} C_{r1}^2 + \frac{241}{16384000} C_{i1} - \frac{29}{1152} C_{i1}^3 - 3C_{i1}^2 C_{i2} - C_{r1}^2 C_{i2} = 0,$$

$$(3.16) \quad \frac{201}{102400} C_{r2} - 2C_{i1} C_{r1} C_{i2} - \frac{29}{1152} C_{i1}^2 C_{r1} - \frac{4879}{16384000} C_{r1} - \frac{29}{1152} C_{r1}^3 - 3C_{r1}^2 C_{r2} - C_{i1}^2 C_{r2} = 0,$$

where $a_{2,1} = C_{r1} + C_{i1}i$ and $a_{2,2} = C_{r2} + C_{i2}i$ are the components of a_2 at $O(\alpha^2)$ and $O(\alpha^4)$ respectively. This gives us a set of four simultaneous equations for the four variables $\{\Re(a_{2,1}), \Im(a_{2,1}), \Re(a_{2,2}), \Im(a_{2,2})\}$, which has five solutions. The first of these solutions,

$$\{0, 0, 0, 0\},$$

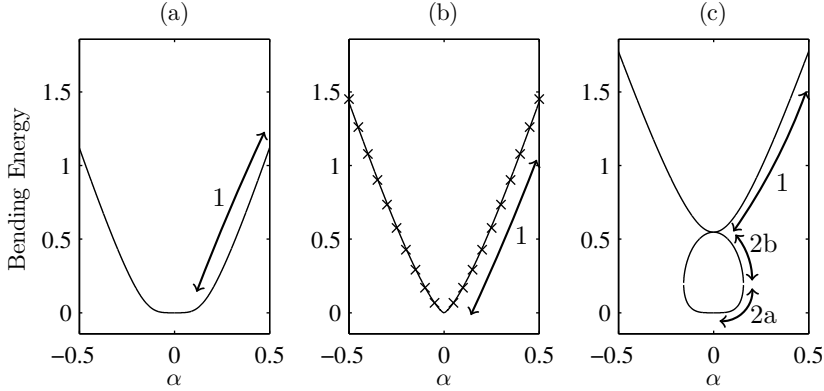


Fig. 6: The bending energy \mathscr{W} near $\alpha = 0$ for (a) $P = 2.9$, (b) $P = 3$ and (c) $P = 3.1$. Panels (a) and (b) show type 1 solutions, and (c) shows type 1, 2a and 2b solutions. The crosses in panel (b) correspond to the asymptotic solution (3.8).

is the same as that predicted for the general case of $P \neq k^2 - 1$, the type 2a solution. The second and third solutions,

$$\left\{ \pm \frac{\sqrt{201}}{320}, 0, \mp \frac{68263}{246988800}, \Im(a_{2,2}) \right\},$$

represent top-bottom symmetric, left-right asymmetric solutions, with one being a left-right reflection of the other. This is the type 3a solution. Note that $\Im(a_{2,2})$ is left undetermined here. The cell-shape is given by

$$(3.17) \quad \eta(\phi) = e^{i\phi} + \frac{\alpha^2}{15} e^{-i\phi} \pm \frac{\sqrt{201}}{320} \alpha^2 e^{-2i\phi} + O(\alpha^4).$$

The fourth and fifth solutions,

$$\left\{ 0, \pm \frac{\sqrt{201}}{320}, \Re(a_{2,2}), \mp \frac{6823}{246988800} \right\},$$

represent left-right symmetric, top-bottom asymmetric solutions, with one being a top-bottom reflection of the other. Here $\Re(a_{2,2})$ is undetermined. This is the type 3b solution. The cell-shape is given by

$$(3.18) \quad \eta(\phi) = e^{i\phi} + \frac{\alpha^2}{15} e^{-i\phi} \pm i \frac{\sqrt{201}}{320} \alpha^2 e^{-2i\phi} + O(\alpha^4).$$

Figure 5 shows the streamlines for these solutions computed using the numerical method discussed in section 3.2. We see that both type 3 cells have the same shape to $O(\alpha^2)$ but with different orientations. However, the fact that $\Re(a_{2,2})$ for the top-bottom symmetric solution is different to $\Im(a_{2,2})$ for the left-right symmetric solution means that both types 3 cells have different shapes to $O(\alpha^4)$.

3.2. Numerical results. We now consider numerically computed solutions to the steady problem. A useful measure for characterising a cell is the dimensionless bending energy \mathscr{W} defined by (2.25). Figure 6 shows the numerically computed bending energy against α for P near 3, as well as the analytical results from §3.1 for $P = 3$. These solutions were described by Blyth & Părău [2], but are included here for completeness. For $P < 3$, we find only type 1 solutions, the vertically aligned top-bottom

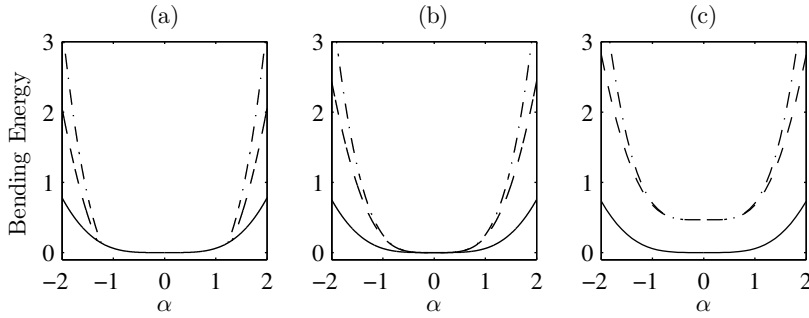


Fig. 7: The bending energy \mathscr{W} near $\alpha = 0$ for (a) $P = 7.9$, (b) $P = 8$ and (c) $P = 8.1$. The solid line indicates type 2a solutions, the dashed line indicates type 3a solutions, and the dash-dot line indicates type 3b solutions.

and left-right symmetric cell shapes. These solution branches have $\mathscr{W} = 0$ at $\alpha = 0$, which corresponds to the circular solution. As P is increased to 3 we see that the energy curve develops a cusp, as predicted by the expansion (3.8). In fact we find excellent agreement between the analytical results and the numerical results. As P is increased above 3, a loop appears in the energy curve underneath the type 1 solution branch, with the lower and upper portions of the loop corresponding to the type 2a and 2b solutions respectively. At $\alpha = 0$, the type 2a solution has $\mathscr{W} = 0$ corresponding to the circular solution, while the type 1 and type 2b solutions have some $\mathscr{W} > 0$ corresponding to the buckled mode-2 solution. As predicted by the analytical results, we find a similar behaviour at $P = n^2 - 1$ for even integer $n \geq 4$. As P is increased through this value, the energy curve with $\mathscr{W} = 0$ at $\alpha = 0$ rises up, crossing $\alpha = 0$ at the buckled mode- n shape. A loop appears underneath this branch which crosses $\alpha = 0$ both at the unit circle solution and at the buckled mode- n solution.

Figure 7 shows the numerically computed bending energy against α for P near 8. As predicted by the analytic results we see that for $P = 8$ there are three solution branches: the type 2a symmetric solution, and the asymmetric type 3a and type 3b solutions. There also exist type 1 and type 2b solutions at $P = 8$, but these have self-intersecting cell profiles, which are non-physical and hence are not shown. The numerically computed values of the bending energy were compared to those obtained analytically, and were found to have excellent agreement for all three solution branches. As P is increased, the type 3a and type 3b branches have $\mathscr{W} > 0$ at $\alpha = 0$, corresponding to the mode-3 buckled cell. But for $P < 8$, the type 3a and type 3b branches do not cross $\alpha = 0$ and instead bifurcate nonlinearly from the type 2a branch at some critical values of $\alpha \neq 0$ which in general are different.

The bifurcation structure can be seen in more detail in Figure 8, which shows the numerically computed bending energies against P for steady solutions with $\alpha = 0$ and $\alpha = 2$. The solid lines represent both the circular and buckled solutions for $\alpha = 0$. For $\alpha = 0$ the steady problem given by (3.1) and (3.2) is rotationally invariant around the origin, and hence the solid lines can be rotated around the P -axis to obtain surfaces of revolution. When $\alpha \neq 0$ the rotational invariance is broken by the flow direction and this creates the imperfections in the bifurcation structure seen in Figure 8. The broken curves either side of the solid branch emanating from $P = 3$ correspond to different orientations of the buckled cell, with the branch on the left corresponding to

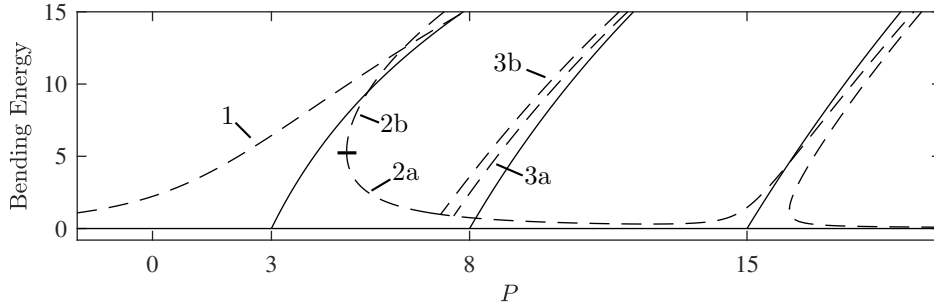


Fig. 8: The bending energy \mathscr{W} against P for steady solutions. The solid line indicates the solutions for $\alpha = 0$, and the dashed line indicates the solutions for $\alpha = 2$. The labels indicate the classification of the $\alpha = 2$ solution branches.

type 1 cells and the branch on the right corresponding to either type 2a (lower part of the branch) or 2b cells (upper part of the branch). The local structure of the solution branches around $P = 8$ is different; in this case the branch that emanates from $P = 8$ for $\alpha = 0$ divides into two and each of these new branches appear as nonlinear bifurcations from a separate branch. In general the local bifurcation structure at the critical points $P = n^2 - 1$ depends on the parity of n : for n odd the behaviour is qualitatively similar to that seen at $P = 8$ in Figure 8, and for n even the behaviour is similar to that seen near $P = 3$ and $P = 15$ in Figure 8.

Figure 9a shows the properties of the type 1 solutions in the $\alpha - P$ plane. These solutions are both top-bottom and left-right symmetric and aligned perpendicular to the flow, as predicted by the linear theory. For $P < 3$, the solutions tend to the circular solution as $\alpha \rightarrow 0$, while for $P > 3$ they tend to the vertically aligned buckled mode-2 solution. As α is increased, the cell pinches together until at some critical value α_c it self-intersects. Solutions for $\alpha > \alpha_c$ are considered unphysical and hence are not considered further. The critical value α_c decreases to $\alpha_c = 0$ as P is increased to $P = 5.247$, with no physically acceptable type 1 solutions beyond this point. These physically meaningful type 1 cells are linearly stable over the region shown in the figure; in fact we have not found any cases for which they are unstable. As $P \rightarrow -\infty$ with $P/\alpha^2 = O(1)$, we obtain the problem for a bubble with constant surface tension in a uniform flow. Nie & Tanveer [9] showed that such solutions are stable for all values of $P/\alpha^2 = (p_\infty - p_0)/(\rho U^2)$. The bubble self-intersects at $P/\alpha_c^2 = -0.273$, so $\alpha_c^2 \sim -3.66P$ as $P \rightarrow -\infty$.

Figure 9b shows the behaviour of the type 2a solutions in the $\alpha - P$ plane. These solutions are both top-bottom and left-right symmetric, and aligned parallel to the flow. As predicted by the analytical results, these solutions only exist for $P > 3$. At $\alpha = 0$ the type 2a cells are circular for $P < 15$ and buckled mode-4 shapes for $P > 15$. Physically acceptable solutions only exist if P exceeds a certain value which depends on α . The type 2a solutions are generally unstable, although there is a large region of stability around $\alpha = 2.8$, $P = 6$.

Figure 9c shows the behaviour of the type 2b solutions in the $\alpha - P$ plane. These solutions are both top-bottom and left-right symmetric, are aligned parallel to the flow, and only exist for $P > 3$. The boundary between the region where solutions exist and the region where solutions do not exist is identical to the one for type 2a solutions, and on this boundary the type 2a and 2b solutions are identical. The type

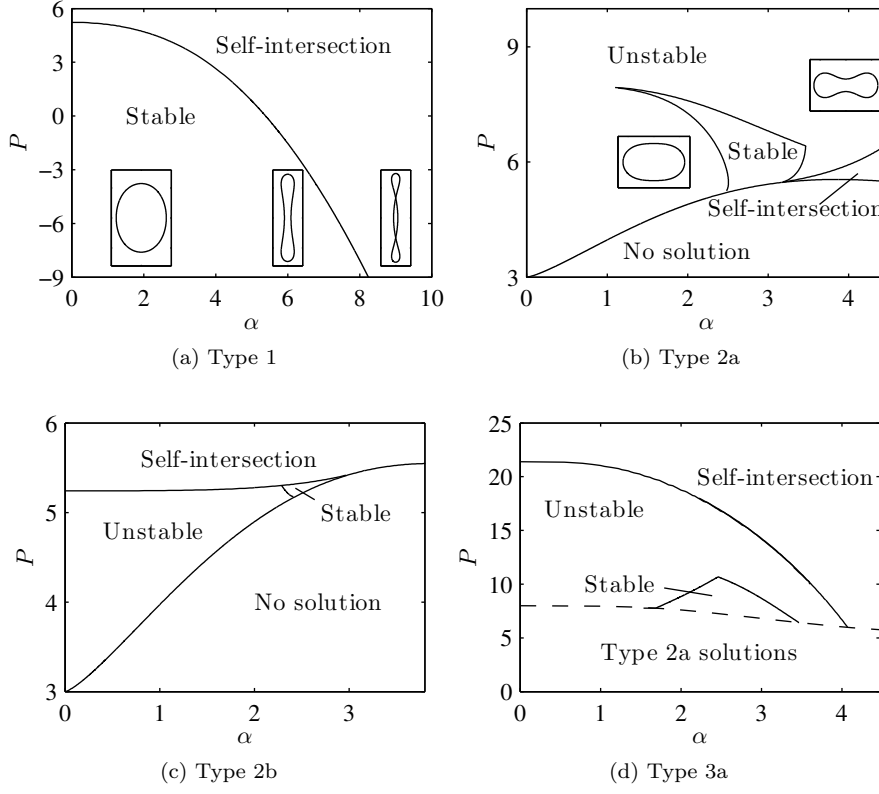


Fig. 9: Properties of the solutions in the α - P plane. The cell shapes shown in panel (a) from left to right correspond to $(\alpha, P) = (2, -6)$, $(6, -6)$ and $(9, -6)$ and in panel (b) from left to right correspond to $(\alpha, P) = (1.5, 6)$ and $(4, 8)$.

2b solutions are unstable except within a very small region of the $\alpha - P$ plane.

Figure 9d shows the behaviour of the top-bottom symmetric left-right asymmetric type 3a solutions in the $\alpha - P$ plane. These solutions exist above the broken line in the figure. Below this line the cells are type 2a solutions which are left-right, top-bottom symmetric, as shown in figure 9b. The type 3a solutions are stable only in a limited region of the $\alpha - P$ plane.

For type 3b solutions, we find that even for cases where the cells are moderately deformed, although the mapping coefficients a_n decay exponentially with n the decay rate is very small, and consequently a large truncation level N is required. This makes the computations for both the equilibrium cells and their stability infeasible for even relatively small values of α and P .

4. Unsteady results. In this section we present simulations of the full unsteady nonlinear equations (2.20)-(2.22). The simulations are used to validate the linear stability results of §2.4 and to describe the evolution of unstable steady solutions of §3 subjected to a small initial perturbation.

Figures 10 and 11 show $\Im(a_1)$ against time for a steady solution perturbed by a stable or unstable eigenvector respectively, for both the linear theory and the nonlinear

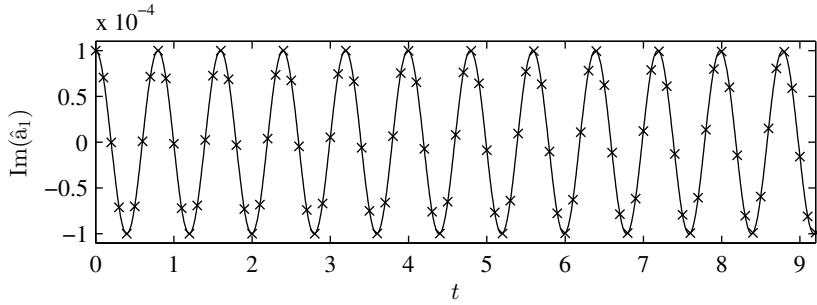


Fig. 10: Results of a time-dependent simulation for a stable steady type 1 solution at $\alpha = 2$, $P = 0$ which is perturbed at $t = 0$ by the stable eigenvector with eigenvalue $\lambda = 7.87i$, scaled by setting $\Im(\hat{a}_1) = 10^{-4}$ and $\Re(\hat{a}_1) = 0$. The solid line shows the numerical calculation and the crosses show the eigenvector.

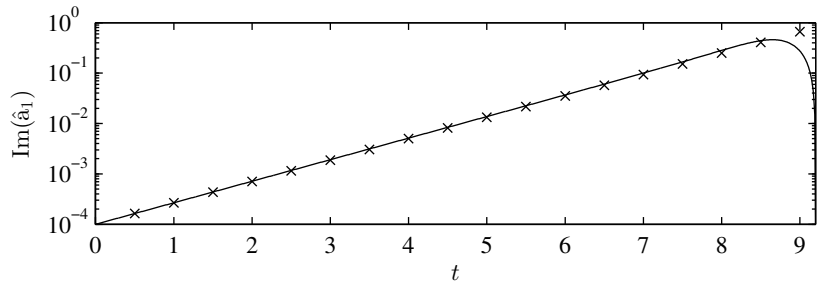


Fig. 11: Results of a time-dependent simulation for an unstable steady type 2b solution at $\alpha = 2$, $P = 5$ which is perturbed at $t = 0$ by the unstable eigenvector with eigenvalue $\lambda = 0.978$, scaled by setting $\Im(\hat{b}_1) = -10^{-6}$. The solid line shows the numerical calculation and the crosses show the eigenvector.

computations. We see that in the stable case the linear theory agrees very well with the nonlinear results for the whole time period considered, and in the unstable case the linear theory agrees well with the nonlinear results until the perturbation becomes too large, after which the evolution becomes fully nonlinear.

The nonlinear time-stepping method can also be used to study the behaviour of the unstable cells as the perturbations become large and nonlinear effects become significant. For near-circular cells whose area is almost π , the constant area and constant perimeter constraints severely restrict the deformation of the cell, causing it to remain near-circular, with the cell motion consisting of small oscillations of the cell wall. For initial conditions corresponding to more deformed steady solutions the unsteady evolution of the cell depends on the number of unstable eigenvectors obtained from the linear stability analysis from §2.4: if there is a single unstable eigenvector, simulations started from initial conditions with different random perturbations will be dominated by the unstable eigenvector in the early stages and lead to nonlinear motions which are qualitatively similar; if there are multiple unstable eigenvectors however, a random initial perturbation will lead to a less predictable motion due to nonlinear interactions of these eigenvectors.

Figure 12 shows the number of unstable eigenvalues for the type 2a cells in the

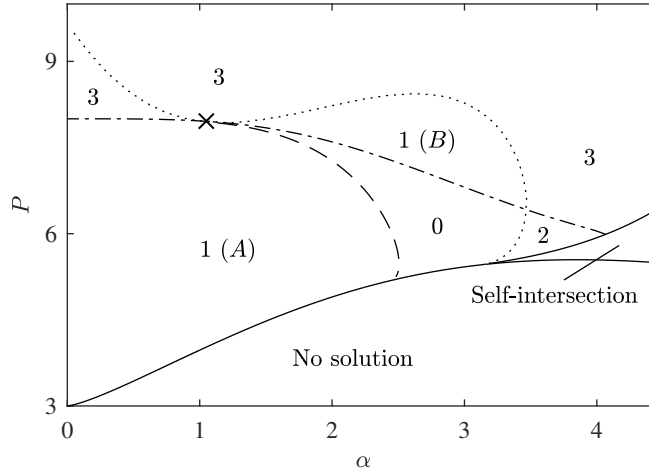


Fig. 12: Map showing the number of unstable eigenvalues for type 2a steady solutions in different regions of the $\alpha - P$ plane where physical solutions exist. On the dashed and dot-dashed lines there is a repeated zero eigenvalue, corresponding to bifurcations of type 3b and type 3a cells from the type 2a cells. On the dotted line there is a pair of repeated real eigenvalues for $\alpha < 1.05$ and a pair of repeated imaginary eigenvalues for $\alpha > 1.05$. The dotted line meets the dashed line at $\alpha = 1.05$, $P = 7.95$, marked by a cross in the map. (A) and (B) mark the two distinct regions with a single unstable eigenvalue.

$\alpha - P$ plane. We note that in general all unstable eigenvalues are distinct and hence have algebraic and geometric multiplicity 1. There are two regions in which the type 2a cell has a single unstable eigenvalue, labelled region A and region B. In region A, the unstable eigenvector rotates the cell, with the direction of rotation determined by the sign of the perturbation. The typical motion of a cell in this region subjected to a small perturbation is sketched in figure 13a. A movie showing a simulation for this cell cycle can be found in the Supplementary Material. As the motion becomes dominated by the unstable eigenvector, the cell rapidly flips over, moving downstream as it does so before holding its position in a near-steady state. It then flips in the opposite direction, again being carried downstream before returning to a near-steady state. The whole cycle is then essentially repeated. However, the motion is not periodic and there are irregular small amplitude oscillations superimposed on the cell wall. We ran a number of simulations in region A and confirmed this general behaviour. This motion is found to also be typical of the unstable type 2b cells, which only ever have a single unstable eigenvalue. Figure 14 shows the horizontal and vertical components of the velocity of the centroid of the cell for a simulation of a specific type 2a cell at $\alpha = 2$, $P = 6$ perturbed by its single unstable eigenvector at $t = 0$. The crosses in the figure show where each frame in the cell cycle in figure 13a occurs. The recurring pattern of cell motion is clearly visible, with the small amplitude oscillations appearing as small irregular bumps in the curve. The alternating direction in which the cell flips can be seen in the vertical component of the centroid velocity, while the horizontal component shows the downstream motion while the cell is flipping.

The typical motion of a cell in region B from figure 12 subjected to a small perturbation is shown in figure 13b. A movie showing a simulation for this cell cycle can

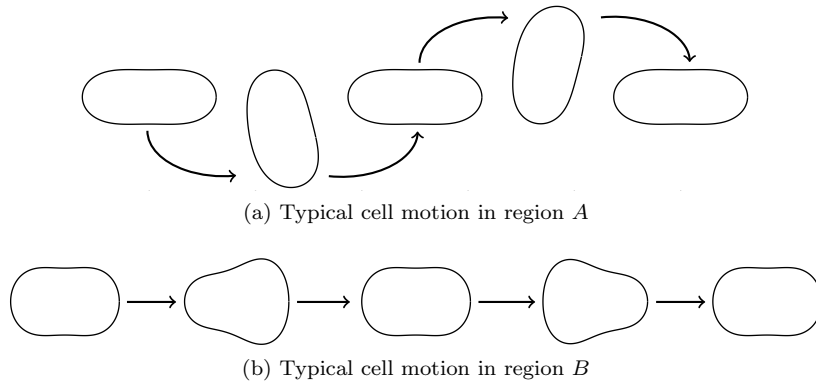


Fig. 13: Sketch demonstrating the nonlinear unsteady motion typical of cells in (a) region A and (b) region B identified in figure 12 subjected to a small initial perturbation, with the leftmost cells depicting initial conditions.

be found in the Supplementary Material. As the motion becomes dominated by the unstable eigenvector, the cell bulges out to resemble a type 3a shape before returning to a near-steady state. During this bulging motion, the cell undergoes intermittent bursts of downstream acceleration, while in between holding its position in a near-steady state. The cell repeats this motion, switching the side to which it bulges in an unpredictable way, with irregular small-amplitude oscillations occurring along the cell wall. We carried out a number of simulations in region B and confirmed this general behaviour. The resemblance to type 3a cells can be explained by noting that the unstable eigenvector corresponds to the eigenvalue associated with the bifurcation from type 2a cells to type 3a cells on the dot-dashed line in figure 12. The downstream motion of the unsteady cells can be explained by use of an energy argument. The bending energy and centroid velocity for a simulation of a specific type 2a cell at $\alpha = 2.5$, $P = 8$ perturbed by its single unstable eigenvector at $t = 0$, are shown in figure 15. Since this initial perturbation is top-bottom symmetric, the cell retains this symmetry throughout the motion, and therefore the centroid velocity is always in the horizontal direction. We see that during the bursts of downstream motion, the bending energy of the cell increases, with a corresponding decrease in the kinetic energy of the flow (2.24). We also see that when the bending energy dips below its initial value, there is a corresponding negative centroid velocity. Since the minimum kinetic energy of the flow corresponds to a cell rigidly translating downstream at speed α , a decrease of kinetic energy generally corresponds to a downstream cell motion.

5. Summary. We have studied an inextensible two-dimensional elastic cell in a uniform flow, with the focus on determining equilibrium states and their stability. Using a conformal mapping approach suggested by Shankar [12] and Tanveer [14] we have computed fully nonlinear equilibria numerically and analysed their stability via an eigenvalue computation as well as time-dependent simulations. We have also used the conformal mapping approach to construct asymptotic approximations valid in the presence of weak flow and confirmed excellent agreement with the numerical computations.

In a study devoted to steady equilibrium solutions, Blyth & Părău [2] used a linearized small- α analysis to demonstrate that a circular cell in a static fluid will

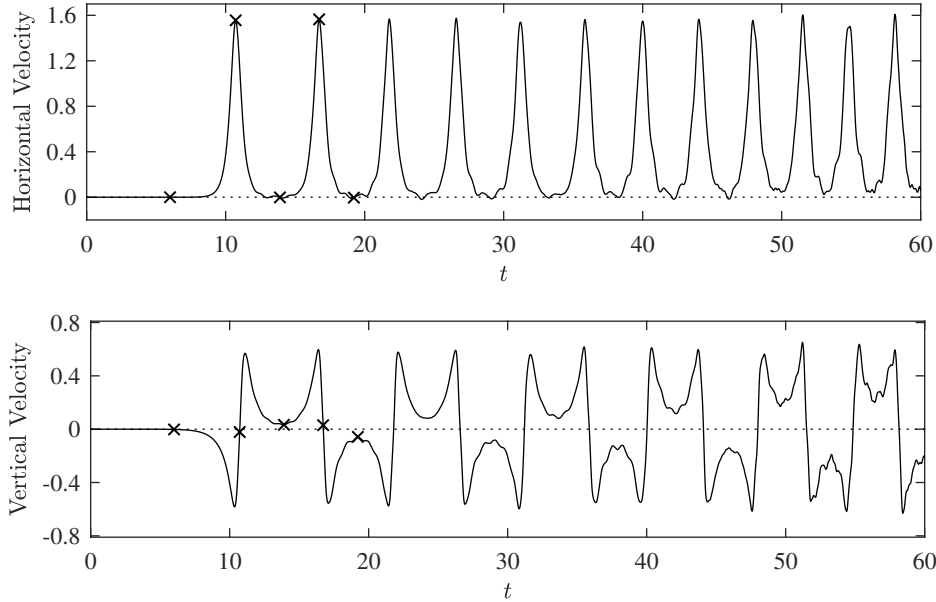


Fig. 14: The horizontal and vertical components of the centroid velocity during the evolution of the unstable type 2a steady solution at $\alpha = 2$, $P = 6$ (region A in figure 12) which is perturbed at $t = 0$ by the unstable eigenvector, with eigenvalue $\lambda = 1.3048$, scaled by setting $\Im(\hat{b}_1) = -10^{-6}$. The dotted line corresponds to the steady solution. The crosses indicate the first five points at which the cell resembles each of the five cells shown in figure 13a. A movie showing the cell shape throughout this simulation can be found in the Supplementary Material.

deform into an elliptical-type shape with its major axis oriented either horizontally aligned with the uniform stream or at ninety degrees to it, depending on whether P exceeds or is below three. This corresponds to the first buckling pressure stated by Flaherty *et al.* [5] for a cell in a stationary fluid. Blyth & Părau's [2] analysis was based on a curvature expansion to first order in α that required knowledge only of the leading order flow around the undeformed cell, and cannot provide details of the first order correction to the flow-field. In the present work we have taken a more natural approach and used a conformal mapping method to enable an expansion in α to be taken to arbitrary order. In doing so we have illuminated parts of the solution space that were missed by Blyth & Părau [2], notably a sequence of critical pressures, that also correspond to those identified by Flaherty *et al.* [5], namely $P = k^2 - 1$ for integer $k \geq 2$, at which further bifurcations are encountered. For example, we have shown for the first time that steady cell shapes with left-right asymmetry and cells with top-bottom asymmetry in the presence of a uniform flow are possible.

We have focused on solutions bifurcating from the first two critical pressures, namely $P = 3$ and $P = 8$ and mapped out the steady solution space in each case. We also carried out a linear stability analysis of the steady solutions and compared the results favourably with time-dependent numerical computations of the full nonlinear system. We found that the horizontally aligned symmetric cells, which exist for $P < 5.247$, are linearly stable for all parameter values that we considered. The vertically

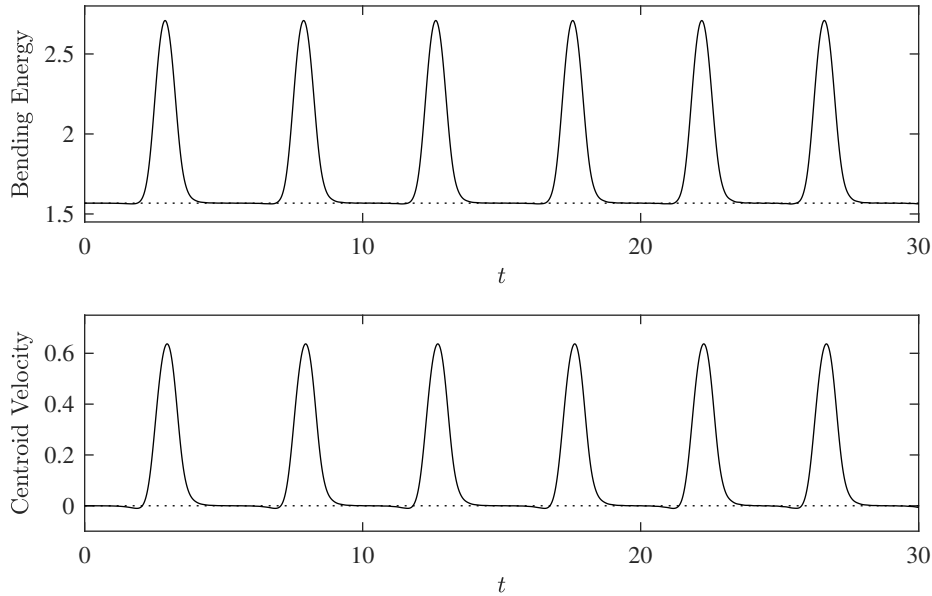


Fig. 15: The bending energy and horizontal centroid velocity during the evolution of the unstable type 2a steady solution at $\alpha = 2.5$, $P = 8$ (region B in figure 12) which is perturbed at $t = 0$ by the unstable eigenvector with eigenvalue $\lambda = 3.7155$ scaled by setting $\Im(\hat{b}_1) = -10^{-4}$. The dotted line corresponds to the steady solution. This motion is top-bottom symmetric, so the centroid velocity has no vertical component. A movie showing the actual cell shape throughout this simulation can be found in the Supplementary Material.

aligned symmetric cells, which exist for $P > 3$, were found to be generally unstable, although we identified some values of the parameters for which these cells were stable. The solutions with a left-right asymmetry were also found to be stable only in a limited region of the parameter space. Finally, we computed the nonlinear time-evolution of the unstable cells subject to a small initial perturbation, and identified regions in which they fall into one of two distinct regular motions, either a flipping motion or a bulging motion, with small irregular oscillations superimposed on the larger scale regular motions. In the flipping motion, the cell flips between near-steady states, with the direction of rotation alternating, but the cell always travelling downstream while flipping. In the bulging motion, the cell bulges out to one side to resemble a top-bottom symmetric mode-3 shape, before returning to a near-steady solution, again travelling downstream during the deformation. In this case the side to which the cell bulges switches in an unpredictable manner.

The conformal mapping approach, which as we have discussed was chosen to facilitate analytic results, proved to be ill-suited for obtaining type 3b solutions. Alternative methods, such as a boundary integral method, may be more appropriate in resolving these solutions. Our analysis of the unsteady dynamics of the system focused on assessing the stability of steady solutions. It would be interesting to perform a more extensive analysis of the unsteady system. Our preliminary calculations have revealed cases where the approximate maximal Lyapunov exponent is positive, indicative of chaos. This motivates further exploration to delineate the regions where

the system is chaotic, and to find periodic or quasiperiodic orbits.

With practical applications in mind, for example the inflatable aerofoils mentioned in the Introduction, it would be desirable to extend the current work to include a trailing edge corner with circulation around the cell producing lift. The present results can then be used as a useful guide to understand the structure of the solution space in this case and allow us to identify equilibrium cell shapes that resemble a traditional aerofoil or have the required aerodynamic capabilities. This is the subject of our ongoing work.

REFERENCES

- [1] J. BAUMGARTE, *Stabilization of constraints and integrals of motion in dynamical systems*, Comput. Methods Appl. Mech. Eng., 1 (1972), pp. 1–16, [https://doi.org/10.1016/0045-7825\(72\)90018-7](https://doi.org/10.1016/0045-7825(72)90018-7).
- [2] M. G. BLYTH AND E. I. PĂRĂU, *Deformation of an elastic cell in a uniform stream and in a circulatory flow*, IMA J. Appl. Math., 78 (2013), pp. 665–684, <https://doi.org/10.1093/imamat/hxt014>.
- [3] G. F. CARRIER, *On the buckling of elastic rings*, J. Math. Phys., 26 (1947), pp. 94–103, <https://doi.org/10.1002/sapm194726194>.
- [4] G. F. CARRIER, M. KROOK, AND C. E. PEARSON, *Functions of a complex variable: Theory and technique*, SIAM, 2005.
- [5] J. E. FLAHERTY, J. B. KELLER, AND S. I. RUBINOW, *Post buckling behavior of elastic tubes and rings with opposite sides in contact*, SIAM J. Appl. Math., 23 (1972), pp. 446–455, <https://doi.org/10.1137/0123047>.
- [6] J. D. JACOB, S. W. SMITH, D. CADOGAN, AND S. SCARBOROUGH, *Expanding the small UAV design space with inflatable wings*, in SAE Technical Paper Series, SAE International, sep 2007, <https://doi.org/10.4271/2007-01-3911>.
- [7] M. LÉVY, *Mémoire sur un nouveau cas intégrable du problème de l'élastique et l'une des ses applications*, J. Math. Pure Appl., 10 (1884), pp. 5–42.
- [8] J. MURRAY, J. PAHLE, S. THORNTON, S. VOGUS, T. FRACKOWIAK, J. MELLO, AND B. NORTON, *Ground and flight evaluation of a small-scale inflatable-winged aircraft*, in 40th AIAA Aerospace Sciences Meeting & Exhibit, American Institute of Aeronautics and Astronautics, jan 2002, <https://doi.org/10.2514/6.2002-820>.
- [9] Q. NIE AND S. TANVEER, *The stability of a two-dimensional rising bubble*, Phys. Fluids, 7 (1995), pp. 1292–1306, <https://doi.org/10.1063/1.868518>.
- [10] C. POZRIKIDIS, *Buckling and collapse of open and closed cylindrical shells*, J. Eng. Math., 42 (2002), pp. 157–180, <https://doi.org/10.1023/a:1015248817797>.
- [11] A. PROSPERETTI, *Advanced mathematics for applications*, Cambridge University Press, 2011.
- [12] P. N. SHANKAR, *On the shape of a two-dimensional bubble in uniform motion*, J. Fluid Mech., 244 (1992), pp. 187–200, <https://doi.org/10.1017/s0022112092003021>.
- [13] I. TADJBAKHSI AND F. ODEH, *Equilibrium states of elastic rings*, J. Math. Anal. Appl., 18 (1967), pp. 59–74, [https://doi.org/10.1016/0022-247x\(67\)90182-5](https://doi.org/10.1016/0022-247x(67)90182-5).
- [14] S. TANVEER, *Some analytical properties of solutions to a two-dimensional steadily translating inviscid bubble*, Proc. R. Soc. Lond. A, 452 (1996), pp. 1397–1410, <https://doi.org/10.1098/rspa.1996.0071>.
- [15] J.-M. VANDEN-BROECK AND J. B. KELLER, *Deformation of a bubble or drop in a uniform flow*, J. Fluid Mech., 101 (1980), pp. 673–686, <https://doi.org/10.1017/s0022112080001863>.